Varying Kinetic Stability, Icosahedral Ordering, and Mechanical Properties of a Model Zr-Cu-Al Metallic Glass by Sputtering

Sachin V. Muley ¹, Chengrong Cao ¹, Debaditya Chatterjee ¹, Carter Francis ¹, Felix P. Lu ^{2,3}, Mark D. Ediger ⁴, John H. Perepezko ¹, and Paul M. Voyles ^{1,*}

¹ Department of Materials Science & Engineering, University of Wisconsin-Madison, 1509 University Avenue, Madison, WI 53706, United States of America

² Grainger Institute of Engineering, University of Wisconsin-Madison, 1550 Engineering Drive, Madison, WI 53706, United States of America

³ Present address – The Pritzker School of Molecular Engineering, University of Chicago, 5640 South Ellis Avenue, Chicago, IL 60637, United States of America

⁴Department of Chemistry, University of Wisconsin-Madison, 1101 University Avenue, Madison, WI 53706, United States of America

Corresponding author: Paul M. Voyles

Author contact information:

Sachin V. Muley (<u>muley@wisc.edu</u>)

Chengrong Cao (ccao32@wisc.edu)

Debaditya Chatterjee (dchatterjee6@wisc.edu)

Carter Francis (csfrancis@wisc.edu)

Felix P. Lu (fplu@uchicago.edu)

Mark D. Ediger (ediger@chem.wisc.edu)

John H. Perepezko (perepezk@wisc.edu)

Paul M. Voyles (paul.voyles@wisc.edu, +1 (608) 265-7273)

Keywords: metallic glass thin films, structure-property relationship, high rate calorimetry, fluctuation electron microscopy, nanoindentation

Abstract

Zr₆₅Cu_{27.5}Al_{7.5} metallic glass thin films with widely varying kinetic stability as a function of deposition rate were synthesized by single-target direct current magnetron sputtering. Fluctuation electron microscopy and angular correlations in coherent electron nanodiffraction show that glasses with increased stability have increased nanoscale structural order, particularly of icosahedral character. The most kinetically stable film's reduced modulus was 22% higher than a glass of the same composition rapidly quenched from the liquid, consistent with increased density and improved thermodynamic stability. These results suggest that enhanced nanoscale icosahedral order contributes both to the kinetic stability of the glass and its resistance to mechanical deformation.

I. Introduction

The same glass composition can exist in a wide variety of thermodynamic states depending on its processing history, including the cooling rate from the liquid to the glass, annealing below the glass transition temperature, T_g , and mechanical work in the glassy state. A particular glass state can be characterized experimentally by its kinetic stability, the resistance to the glass transition quantified by T_g measured on heating, and its thermodynamic stability, quantified by the enthalpy. Annealing (or aging) increases kinetic stability and decreases enthalpy. Swallen *et al.* showed that physical vapor deposition (PVD) can create glass films of molecules with such high kinetic stability and such low enthalpy that it would require thousands of years to achieve by annealing [1]. The exceptional stability arises from high molecular mobility in the first few monolayers near the film surface during growth, combined with long surface residence times created by low deposition rates [2]. Their results spawned efforts to create ultrastable glasses in other materials systems, including metallic glasses [3–11], polymer glasses [12] and chalcogenide glasses [13], and to connect the properties of these novel materials to their structure and thermodynamic state.

Previous studies of increasing the stability in metallic glass thin films using PVD have yielded intriguing but conflicting results, although substrate temperature [3–7] and deposition rate [9,10] are clearly the controlling synthesis parameters. Using sputtering, Yu *et al.* [3] showed higher kinetic stability and higher enthalpy, which is not typical glass behavior, in $Zr_{65}Cu_{27.5}Al_{7.5}$ at a deposition temperature of $0.8T_{onset}$, where T_{onset} is the temperature at the start of the glass transition measured on heating of a reference bulk glass sample. In contrast, Aji *et al.* [4] showed both higher kinetic stability and lower enthalpy at a deposition temperature of $0.8T_{onset}$ in $Zr_{55}Cu_{30}Ni_{5}Al_{10}$. In $Pd_{77.5}Cu_{6}Si_{16.5}$, Magagnosc *et al.* [5] observed that the elastic modulus and

hardness as a function of deposition temperature peaked at $0.73T_{onset}$, which they interpret as evidence of lower enthalpy. Liu et al. [6] reported higher elastic modulus, suggesting higher density and lower enthalpy, but reduced kinetic stability with increasing deposition temperature in Zr-Cu-Ni-Al-Hf-Ti films. For Zr-Cu-Ni-Al films, Chu et al. [7] showed improved mechanical properties with increasing substrate temperature, but kinetic stability for all films was unchanged. Using ion-beam assisted deposition (IBAD) to achieve very low deposition rates, Luo et al. [9] and Liu et al. [10] showed that lowering the deposition rate by an order of magnitude resulted in large increases in kinetic stability of deposited films, but neither reported enthalpies. Sun et al. [14] report smaller but still significant changes in kinetic stability by changing deposition rate in sputtering of Zr-Cu-Al and Zr-Cu-Al-Mo films deposited at room temperature and show that more kinetically stable glasses have a shorter length scale for heterogeneity in their mechanical dissipation measured by amplitude-modulated atomic force microscopy. They interpret the shorter length scale as evidence of a more homogeneous structure in the more stable glasses. On balance, PVD seems to be an effective tool for creating metallic glasses with varying stabilities, creating novel opportunities to explore a wide spectra of glass structure and establish structure-property relationships, but the relationships between synthesis parameters and stabilities are unclear.

Although the general structure features of Zr-Cu based metallic glasses are well-established, especially at short range, the structural features of glass packing responsible for wide variations in stability, at constant composition, are not as well understood. Bulk glasses of Zr-Cu and related alloys have short-range order dominated by icosahedral Voronoi polyhedra, which are often distorted [15–17]. The icosahedra tend to have Cu or other small atoms at their centers [15]. Medium-range order consists of connected clusters of icosahedra [18–20] or crystal-like clusters identified by their four- and six-fold rotational symmetry [20,21]. The films discussed above have

been studied with conventional structural means such as laboratory x-ray diffraction and highresolution TEM, but those methods primarily confirm that the materials are amorphous. Luo *et al.*used synchrotron x-ray diffraction to measure the total pair distribution function G(r), which
showed enhanced structure at large r, suggesting some form of nanoscale ordering, and a small
shift of the low-r peaks to smaller r consistent with densification [9]. Aji *et al.* interpret small
changes in the synchrotron G(r) at low r as evidence of enhanced chemical ordering with increased
stability [4]. They also used electron nanodiffraction in the form of Ångstrom beam electron
diffraction [22] to demonstrate that their films do not contain even nanometer-diameter crystals,
and that the short-range order is consistent with molecular dynamics simulations. Taken together,
these results show that there are changes in structure associated with stability that extend from
nearest-neighbor length scales to up to nearly 1 nm, but they do not identify clearly what the
structure might be.

Here, we use deposition rate in PVD to manipulate the stability of Zr₆₅Cu_{27.5}Al_{7.5} metallic glass films, creating materials both more stable than and similar in stability to liquid-quenched glass with the same composition. We demonstrate using electron nanodiffraction fluctuation microscopy and angular correlations that enhanced stability is correlated to increased nanometer-scale medium-range order in this material, which has a marked icosahedral character. We also show that improved kinetic stability coincides with increased modulus measured by nanoindentation, suggesting improved thermodynamic stability as well.

II. Experimental Section

Following Yu *et al.* [3], we have synthesized Zr₆₅Cu_{27.5}Al_{7.5} films using single alloy target magnetron sputtering at varying substrate temperatures and varying deposition rates. Thin films

were deposited by employing an in-house built high vacuum direct current magnetron sputtering tool. An arc-melted alloy target with nominal composition of Zr₆₅Cu_{27,5}Al_{7,5} (at. %) was purchased from Haohai Metal Materials Co. Ltd., China. The base pressure of the vacuum vessel was better than 5×10^{-8} Torr with partial pressures of oxygen of 2×10^{-10} Torr and water vapor of 5×10^{-9} Torr as measured by an SRS 100 residual gas analyzer. The operating pressure of Ar process gas was 5 mTorr during deposition as measured by KJLC 275i convectron gauge. The target was presputtered for 1 minute to remove surface oxide and allow the vapor to achieve steady-state composition. A range of thin films were grown at deposition rates from 0.24 nm/s to 1.19 nm/s and substrate temperatures from 0.693 T_g (443 K) to 0.707 T_g (453 K). 500 - 650 nm thick films were grown on chemical vapor deposited 220 nm-thick amorphous Si₃N₃ on 001 Si substrate for X-ray diffraction (Bruker D8 Discover with $Cu-K_{\alpha}$ source), scanning electron microscopy and energy dispersive spectroscopy (Zeiss Leo-1530), differential scanning calorimetry (Mettler Toledo Flash DSC 2+), and nanoindentation (Hysitron TI 950 Triboindenter). Approximately 20 nm thick films were grown on electron transparent 15 nm thick Si₃N₄ membranes for FEM (FEI Titan 80-200, operated to 200 KV with a 0.6 mrad convergence angle, 2 nm diameter probe) studies. Quenched amorphous ribbons with nominal composition of Zr₆₅Cu_{27.5}Al_{7.5} (at. %) and thickness of $30 - 40 \mu m$ were made by melt-spinning for comparative nanoindentation studies. See Supplemental Material at < URL to be inserted by publisher> for complete experimental and data analysis details [23]. All references from Supplemental Material are listed here [20,24–27].

III. Results

A. Structural characterization by XRD

Fig. 1(a) shows XRD traces from films deposited at deposition rates of 0.24, 0.83, and 1.19 nm/s and at substrate temperatures of 443 to 453 K (0.700 \pm 0.007 T_{onset} of reference liquid-

quenched ribbon as measured by conventional calorimetry). Films grown at higher temperatures were all crystalline, regardless of the deposition rate. Fig. 1(a) shows a first broad diffraction peak at $36.7 - 36.9^{\circ}$ and a second broader halo at higher angles. The full width at half maximum (FWHM) of the first peak ranges from 5.24° to 5.64° , depending on the deposition parameters, as shown in Fig. 1(b), which corresponds to a scattering vectors magnitude q of ~ 0.37 Å⁻¹ – 0.40 Å⁻¹ ($q = 4\pi \sin \Theta / \lambda$, where λ is X-ray wavelength, 1.5418 Å). These values are close to values reported for BMGs ($\sim 0.4 - 0.5$ Å) [28], confirming that the peaks are amorphous by this measure. For amorphous thin films, the position of the first peak is nearly constant at $36.7^{\circ} \pm 0.04^{\circ}$, similar to the value for the ribbon of 36.9° , as seen in Fig. 1(c). Energy dispersive spectroscopy (Fig. A1) shows constant composition for all the films within experimental uncertainty.

B. High rate calorimetry

Fig. 2 shows representative calorimetry data measured at a heating rate of 5000 K/s for the same films and ribbon. We report glass transition onset temperatures T_{onset} estimated by the standard tangent method for all samples. Fig. 2(a) shows that the slower deposited films (0.24 nm/s and 0.83 nm/s) have enhanced kinetic stability as shown by a T_{onset} increase of 25 ± 5 K compared to the bulk ribbon sample. The film deposited at 1.19 nm/s has nearly the same T_{onset} as the ribbon sample within experimental error. This trend in T_{onset} with respect to deposition rate is also observed for DSC measurements at heating rates of 1000 and 2000 K/s (not shown). All the reported T_{onset} data are higher than previous reports on similar compositions using conventional DSC, partly because of the high heating rate. High thermal rate DSC is advantageous compared to conventional DSC for these experiments because it enables experiments on relatively thin films, avoiding the very long depositions required to make sufficiently thick films to accumulate the few milligrams necessary for conventional DSC.

Figure 2(b) shows Kissinger analysis on a liquid-quenched ribbon sample at heating rates of 0.33 K/s, 1.67 K/s and 5000 K/s and the slowest deposited film at heating rates of 1000 K/s, 2000 K/s and 5000 K/s. Although the uncertainties are large, the results suggest that the activation energy to transform the glass into the supercooled liquid in the slowest deposited film $(4.2 \pm 1.5 \text{ eV})$ might be higher than for the ribbon $(2.6 \pm 0.4 \text{ eV})$. Extrapolating the Kissinger analysis for the films to lower heating rate of 1.67 K/s gives T_{onset} of 680 K for the film deposited at 0.24 nm/s, as against 640 K measured for the ribbon at 1.67 K/s. Our results seem qualitatively consistent with other studies in the literature that focused on the effect of heating rate on metallic glasses, both in thin film [29,30] and bulk forms [31–33].

The crystallization signature in DSC is shown in Fig. 2(c). The ribbon shows a single crystallization peak with a well-defined supercooled liquid region, but all the films show two crystallization exothermic peaks and a lower crystallization onset temperature. The first crystallization event and the lower onset temperature may result from heterogeneous nucleation of crystals at the film surface for the relatively thin films (< 1 µm) we have studied. The second event, which occurs at approximately the same temperature as the crystallization of the ribbon, is then bulk crystallization from the interior of the film [29,34].

C. Fluctuation electron microscopy and angular correlations

Fig. 3 shows electron nanodiffraction structural characterization results for a set of thinner films directly deposited onto electron-transparent Si_3N_4 substrates at the same temperature as a function of deposition rate. A high coherence, focused electron beam 2 nm in diameter in a scanning transmission electron microscope (STEM) was used to measure nanodiffraction patterns from many positions on the sample. One example pattern is shown in Fig. 3(e). FEM measures the

spatial fluctuations in the diffracted intensity using the normalized variance V of the spatially resolved intensity I as a function of scattering vector magnitude k and the coherent spatial resolution R [35]

$$V(k,Q) = \frac{\langle l^2(k,Q,R) \rangle}{\langle l(k,Q,R) \rangle^2} - 1,$$
(1)

where <> indicates averaging over position on the specimen. Quantitatively, V depends on the three- and four-atom position correlation functions. Qualitatively, structural variations at the nanoscale increase V(k), and the position of peaks in k reveal internal atomic arrangements within strongly diffracting regions. Fig. 3(a) shows the V(k) data, with error bands representing the standard deviation of the mean of V(k) computed from at least 10 different areas of the sample. All the samples have a broad peak centered near $\sim 0.40 \text{ Å}^{-1}$. The slower deposition rate samples (0.24 nm/s and 0.83 nm/s) have a low-k shoulder at $\sim 0.36 \text{ Å}^{-1}$. There is an additional high-k feature in the faster deposition rate sample (0.83 nm/s and 1.19 nm/s) at 0.46 or 0.48 Å⁻¹, respectively, and there may be a small feature near $\sim 0.42 \text{ Å}^{-1}$, although it is not outside the errors bars of the data.

Fig. 3(b)-(f) shows the power spectrum of angular correlations calculated from the same set of nanodiffraction patterns, which complicates and expands this structural picture. Angular correlations and their power spectrum probe the approximate rotational symmetries exhibited by the nanoscale structure of a glass [16,17]. To compute the angular correlations, the nanodiffraction patterns first were converted to polar coordinates (k, ϕ) as defined in Fig. 3(e) and corrected for a small elliptical distortion, probably from residual diffraction astigmatism. Then the angular autocorrelation function

$$C(k,\phi) = \frac{\langle I(k,\theta+\phi) I(k,\theta) \rangle_{\theta} - \langle I(k,\theta) \rangle_{\theta}^{2}}{\langle I(k,\theta) \rangle_{\theta}^{2}}$$
(2)

was calculated for every pattern, where $<>_{\theta}$ indicates averaging over θ . $C(k, \phi)$ was averaged over many sample position, then finally, Fourier transformed to find the angular power spectrum as a function of k and rotational symmetry order n. An example power spectrum computed from the pattern in Fig. 3(e) is shown in Fig. 3(f). This pattern was selected out of the data set to show strong n = 10 symmetry.

The angular power spectrum should identify rotationally symmetric, ordered structures since the diffracted intensity from ordered regions is stronger and more directional than the diffuse diffraction from disordered regions [37]. However, previous angular power spectrum results contain significant odd-n components which are inconsistent with Friedel symmetry in diffraction and have been criticized as unphysical [36]. These odd-n features have recently been shown to be artifacts from TEM samples that are too thick [38], presumably arising from chance alignments of speckles arising from different structures that overlap through the projected thickness of the TEM sample. Our samples are sufficiently thin to limit these artifacts. Fig. A3 shows all angular power spectra for n = 1 to 10 for all the films, showing that the even n power is systematically larger than the odd n-1 or n+1 powers. Ignoring the n=1 power created by isolated, single speckles, the ratio of even n power to odd n power ranges from 1.5 to 1.9 for the three samples.

Fig. 3(b)-(d) show the power spectrum of the summed angular correlations for 4-, 6- and 10-fold symmetries respectively, with error bands representing the standard deviation of the mean of P(k, n) computed from at least 10 different areas of the sample. The slowest deposition rate, 0.24 nm/s sample shows substantially more structure in the 4-, 6-, and 10-fold power spectra than the other two samples, and it has the highest ratio of even to odd total power at 1.9. For the slowest rate sample, P(k, n=4) has clear peaks at 0.36, 0.39, and 0.438 Å⁻¹, P(k, n=6) has peaks at 0.385 and 0.42 Å⁻¹, and P(k, n=10) has peaks at 0.37 and 0.42 Å⁻¹. The fastest deposition rate, 1.19 nm/s

sample shows the least structure in P(k, n). There are broader peaks near $k = 0.40 \text{ Å}^{-1}$ for n = 4, 6, and 10, and features in P(k, n=4) near 0.42 and 0.475 Å⁻¹. The intermediate rate, 0.83 nm/s sample, has intermediate features in P(k, n), including a small feature in P(k, n=10) near $k = 0.36 \text{ Å}^{-1}$. The ratio of even to odd power is 1.51, somewhat smaller than the fastest rate sample.

D. Mechanical properties

Fig. 4 shows the reduced elastic modulus (E_r) and hardness (H) as a function of T_{onset} values for the films and the ribbon. All the films have higher E_r than the ribbon, and the film E_r increases 5% with T_{onset} . At constant composition, E is related to the interatomic potential U, average atomic radius r_0 , and the bonding length between two atoms r by $[7]E = \frac{1}{r_0}\left(\frac{1}{r}\left(\frac{dU}{dr}\right)\right)$. The small variation in measured composition of ± 2 at. % shown in supplemental Fig. A1, even if it is real and not composition measurement uncertainty, accounts for at most a 0.8% variation in modulus, as estimated by composition-weighted averages of the elemental moduli. For the thin films, H increases by 14% with decreasing deposition rate and increasing T_{onset} . The difference in hardness between the slowest 0.24 nm/s film and the ribbon reference sample is 3.8%. We also tested an \sim 3 μ m thick film grown at a deposition rate of 0.83 nm/s to test for sample size effects on the glass's mechanical response. The results were consistent within experimental uncertainty with results on the thinner film grown at same deposition condition.

Fig. 5 compares images of indents made at a peak load of 1.5 mN in the ribbon and the thick, 0.83 nm/s film. Fig. 5(a) and (b) show gradient force images (scanning set point error), and Fig. 5(c) and (d) show two-dimensional surface maps. The indents in the ribbon are surrounded by pileups, but not pileups are observed for the film indents film. This difference in pileup behavior was consistent up to higher peak loads of 16 mN, and images (not shown) of indents in the thinner

films also showed no pileups.

IV. Discussion

The FEM data show that the film's structure grows more icosahedral with decreasing deposition rate and as the films increase in T_{onset} and grow more kinetically stable. Previously, in bulk Zr-Cu-Al metallic glasses, we have used FEM data and hybrid reverse Monte Carlo (HRMC) modeling to show that the low-k shoulder on the main V(k) peak, near $k = 0.36 \text{ Å}^{-1}$ in Fig. 3(a), arises from icosahedral ordering, and the main peak $(k = 0.40 \text{ Å}^{-1})$ and the high-k shoulders $(k = 0.40 \text{ Å}^{-1})$ $0.44 - 0.48 \text{ Å}^{-1}$) arise from crystal-like order [20,21]. Icosahedral order in the HRMC models is identified as regions with icosahedral or quasi-icosahedral Voronoi polyhedra and local, approximate five-fold rotational symmetry. "Crystal-like" order is identified by regions with approximate six-fold rotational symmetry [20,21]. Electron diffraction data are not directly chemically sensitive, so we cannot discern whether shifts in structure are related to chemical ordering as previously reported [4]. Shifts in the V(k) peak positions occur because the geometry of different types of clusters produces different pseudo-planar alignments of atoms which give rise to strong speckles in nanodiffraction [21]. Interpreted in the same way, Fig. 3(a) shows that all of the films have both icosahedral and crystal-like nanoscale structural order, but that the lower deposition rate films, especially the lowest rate, 0.24 nm/s film, have stronger icosahedral nanoscale order than the high deposition rate film, as shown by the higher V at $k = 0.36 \text{ Å}^{-1}$. The two higher rate films have relatively stronger crystal-like order, given the high-k features, than the lowest rate film, which has no features at $k > 0.40 \text{ Å}^{-1}$.

The angular symmetries reinforce and expand this finding. The angular symmetries show that the structural order in the slowest sample is both icosahedral and crystal-like. 10-fold symmetry arises only from icosahedral order, so peaks in P(k, n=10) confirm icosahedral ordering.

4-fold symmetry arises only from crystal-like order, so peaks in P(k, n=4) confirm crystal-like ordering. 6-fold symmetry can arise from either crystallographically-allowed 6-fold symmetry, Friedel doubling of crystallographically-allowed 3-fold symmetry or doubling of diffraction from the 3-fold symmetry axis of an icosahedron. As a result, the peaks in P(k, n=6) are hard to assign uniquely, but the lower k position of the main peak compared to the data for the other two samples suggests a different structural origin, pointing perhaps to icosahedral instead of crystal-like structures. Combined with the FEM data, these results suggest contribution of a stronger icosahedral character to the nanoscale order in this sample. Unlike the FEM results, this result does not depend on structural modeling. Instead, it is derived directly from rotational symmetries in the data. The higher overall magnitude of P(k, n) for the slowest sample shows that this sample has, on average, brighter, more symmetric speckles in nanodiffraction than the other two samples, suggesting that its well-ordered, strongly diffracting regions occur at higher density, have more perfect internal order, or are larger, or some combination of all three. Angular symmetry mapping with a fast detector might distinguish these scenarios [38], but the spatial sampling of the current data is not sufficient for that type of analysis.

For the fastest deposition rate sample, the features in P(k, n=4) are consistent with the assignment of features in V(k) at similar k to crystal-like order, and suggest that on balance this sample has more crystal-like character to its order. The ratio of even to odd order power is 1.61, and much of that power is concentrated in P(k, n=2), suggesting less overall order and either smaller or less internally structured ordered regions. The intermediate rate, 0.83 nm/s sample is also intermediate in structural order. The small feature in P(k, n=10) near k=0.36 Å⁻¹ is consistent with V(k) and icosahedral ordering, but not as pronounced as the slowest rate sample. It does not show a similar peak in P(k, n=4), indicating substantial crystal-like order.

The mechanical property results are consistent with increased stability of the glass at lower deposition rate. An increase in E can result from a shortened average interatomic distance and a denser glass structure, making it a proxy for glass thermodynamic stability [3,5,39]. The modulus results suggest that all the films have higher thermodynamic stability than the ribbon sample. The mechanical energy needed for onset of plasticity has been related to the glass fictive temperature, T_f , which is another, indirect measure of thermodynamic stability [40]. The change in fictive temperature is $\Delta T_f = -\Delta \sigma_y V / \Delta C_{lg}$, where $\Delta \sigma_y$ is the change in yield strength, V is the molar volume, and ΔC_{lg} is the difference in heat capacities of the supercooled liquid and the glass extrapolated to a temperature below T_g . T_f is then related to the enthalpy required for the glass transition by $\Delta H =$ $\Delta T_f \Delta C_{lg}$ [40]. For our composition, $\Delta C_{lg} = 23.6$ J/mol.K [3] and the molar volume is 11.4 cm³/mol. With a Tabor factor of 1/3, $\sigma_y = H/3$ [41]. If we compare the 0.24 nm/s slowest rate film to the 1.19 nm/s fastest rate film, $\Delta T_f = 116 \pm 5$ K and $\Delta H = 2.7 \pm 0.1$ kJ/mol, derived from the hardness. These changes are significantly larger than examples previously reported changes in T_f (~ 75 K) and H (~ 1.5 kJ/mol) created by thermal aging in Zr-based glasses [42,43] measured by calorimetry. The difference in hardness between the slowest 0.24 nm/s film and the ribbon reference sample is 3.8%, which results in $\Delta T_f = 35 \pm 5$ K and $\Delta H = 0.9 \pm 0.1$ kJ/mol. We suggest the hardness differences between slower deposited films and reference ribbon sample may still be underestimated due to the influence of microstructure between the ribbon and the films, including surface roughness (Fig. A2) and the possibility of columnar growth [44,45].

Part of the motivation for this work was to attempt to replicate and expand on the previous work of Yu et al. on the same glass forming system [3]. While we have replicated their results in general by using sputtering to manipulate the stability of same composition metallic glass thin film, we do not replicate the results in detail. Films we grew at the same substrate temperatures

they used (> 0.707 T_{onset}) were crystalline, not amorphous, but the fractional change in T_{onset} we find for our glassy films as a function of deposition rate at lower substrate temperature is twice what they reported. This result points to a need for significantly improved process control over key parameters that could include the chamber base pressure and residual gas composition, process gas pressure and trace contaminants, plasma energy density at the sample, etc., if enhanced stability metallic glass coatings are to see reliable use in applications.

The changes in stability we report are smaller than those reported by Luo et al. [9] and Magagnosc et al. [5]. Luo et al. [9] report a 8.5% T_{onset} increase for a one decade reduction in deposition rate, but we observe a 3.3% T_{onset} increase for ~ 0.7 decade of deposition rate. This difference may arise because IBAD enables overall one decade lower deposition rates than our work and has a more energetic plasma (100 - 2000 eV) than sputtering (1 - 100 eV) [46], which might densify the film or enhance surface mobility. Organic glass films exhibit a significantly weaker dependence of kinetic stability of deposition rate, with a 5% increase in T_{onset} reported from a two decade reduction in deposition rate [47]. We suggest this difference is connected to the fragility, m, of the different glass systems, which is 80-90 for indomethacin and 40-50 for Zr-based MGs [3]. Magagnosc et al. [5] reported ΔT_f of 333 K and ΔH of 6.19 kJ/mol for a Pd-Si-Cu glass films by substrate temperature control, which is very large, but that results reflects the reduced stability possible in deposited films at low temperature, as well as enhanced stability at high temperature, and not the difference to a quenched glass reference. The influence of stability on crystallization onset temperature is also complicated. We observe a lower crystallization temperature with higher stability, probably due to surface crystallization. Yu et al. [3] reported nearly the same crystallization temperatures for their ultrastable glass and bulk ribbon, and Luo et al. [9] and Aji et al. [4] both observed higher crystallization temperatures with enhanced stability.

More generally, sputtered metallic glass films often have different crystallization pathways than bulk glasses [44,48], so this is an area which requires additional research.

Changing a glass's stability changes its structure and mechanical properties. In structure, the results on film samples here fit within a picture we have previously developed for Zr-Cu-Al glasses in which icosahedral and crystal-like order compete at the nanoscale. Previously, we had shown that changes in composition which increase glass-forming ability (from Zr₅₀Cu₃₅Al₁₅ to $Zr_{50}Cu_{45}Al_5$) also increase both the prevalence of icosahedral order and its stability under sub- T_g annealing [20,21]. In those experiments, changes in enthalpy and T_{onset} were dominated by the changes in bond energies arising from changes in composition, rather than arising from changes purely in structure. Here, we show similar behavior, but at constant composition: increased order at the nanoscale gives rise to overall increased stability, and that order tends to be icosahedral. The higher modulus and hardness observed here are consistent with higher density at low deposition rate and higher substrate temperature, as observed in other materials [39]. The higher density is accommodated by denser atomic packing, leading to increased nanoscale structural order. Molecular dynamics simulations of vapor-deposited Zr-Cu-Al glass films also show that more stable glasses have a markedly higher fraction of icosahedral nearest-neighbor clusters than simulated glasses created by quenching from a liquid [49]. Also in molecular dynamics simulations, nearest-neighbor icosahedral clusters exhibit slower dynamics than other clusters in the liquid [50], greater resistance to local transformations in structure, and increased heat capacity and barrier to crystallization in the glass [51,52], all of which is consistent with increased icosahedral order leading to increased T_{onset} , as observed.

Lack of pileup around the film indents is likely a sign of homogeneous plastic deformation and suggests brittle failure. The amorphous structure is intrinsically heterogeneous and large

clusters of inherent defects can be fertile sites for percolation of shear transformation zones [53]. Simulations show more icosahedral ordering can cause higher resistance to shear transformation zones' activation and operation, reducing the chance for localized plastic flow and promoting homogeneous plastic deformation [53]. On the other hand, material pileup in Zr-based bulk glass samples is well documented, indicating the plastic deformation is localized and dominated by heterogeneous nucleation, resulting in subsequent sliding of shear bands as governed by exceeding a critical flow stress [54,55]. Our results are in contrast Magagnosc *et al.* [5], who reported shear banding for their more stable glassy films.

Simulations also support the connection between icosahedral ordering and higher strength, [56–58] measured here as higher hardness. Peng *et al.* [57] showed in CuZr that local five-fold rotational symmetry in the structure is correlated to reduced non-affine displacement under strain, meaning that five-fold symmetric local structures (including icosahedra) were harder to deform than other parts of the glass structure. They also showed that plastic deformation started at regions with low five-fold order and proceeded towards regions with high five-fold order. Cheng et al. [56] reported that mechanical properties in CuZr MGs have a structural origin in the relative populations of icosahedra and liquid-like clusters, with more icosahedral clusters leading to lower potential energy and stronger resistance to deformation. If a MG has more liquid-like clusters than the percolation limit, the glass-to-liquid transition will be easier resulting in poorer mechanical properties [58]. We suggest that the liquid-like clusters in their simulations have reduced structural order compared to the rest of the glass, so the overall enhanced order we observe may relate to a reduction in the concentration of liquid-like clusters, consistent with the increased hardness.

V. Conclusions

In summary, we report that kinetic stability of sputtered metallic glass thin films can be controlled by the deposition rate at constant substrate temperature from stability similar with liquid quenched glasses to significantly more stable. Structural studies using electron nanodiffraction show that the improved kinetic stability originates from increased nanoscale order in the glass, especially in the form of nanoscale clusters of icosahedra. Modulus and hardness both increase with increasing kinetic stability, suggesting that the higher kinetic stability also means higher density and lower enthalpy. These results show that increased icosahedral nanoscale order increases the resistance of the glass to changes in structure, either thermally in the form of the glass transition or mechanically in the form of plastic deformation. These correlations are drawn entirely at constant composition, so they derive purely from changes in structure without the complexities of changes in bond strength caused by changes in composition.

Supporting Information

Software for angular correlation analysis of electron nanodiffraction is available in the open source pyXEM package (https://github.com/pyxem/pyxem). Data and images presented in figures and all the raw data analyzed to produce those plots is available from the Materials Data Facility (DOI: 10.18126/xa3c-69j6).

Acknowledgments

This research was primarily supported by National Science Foundation (NSF) through the University of Wisconsin Materials Research Science and Engineering Center (DMR-1720415), including sample synthesis, thermal and mechanical analysis, and structural characterization. Additional support for development of angular correlation analysis by C.F. was provided by NSF DMR-1807241. The authors gratefully acknowledge the use of facilities and instruments supported

by NSF through the University of Wisconsin MRSEC (DMR-1720415). Stimulating discussions with Prof. Lian Yu and Prof. Donald Stone are highly appreciated.

Appendix

A. Composition and microstructural characterization

Fig. A1 summarizes measured elemental composition by EDS of the films, the sputter target and the liquid-quenched ribbon. The error in each measurement is the standard deviation in EDS measurements at five different spots. The results suggest that for films grown at different deposition conditions, the composition difference is within 1%, while the bulk ribbon and target differ by 2%. The variations in composition are too small to account for the differences in T_{onset} .

Figure A2 shows SEM and AFM images of all the three samples. The microstructure is generally columnar. The 0.24 nm/s and 0.83 nm/s samples have a similar root mean square (rms) roughness of 3.7-3.8 nm and a similar roughness length scale (~ 70-90 nm), based on AFM and SEM images. The 1.19 nm/s sample on the other hand shows a bimodal distribution of a few large hillocks (~ 110 nm) distributed in a matrix of smaller ones (~ 45-50 nm). It also has a smoother surface, with an rms roughness of 1.6 nm. The mean hillock size, determined by applying the grain-intercept image analysis method used to determine crystal grain sizes, is 66, 71, and 73 nm for the 0.24 nm/s, 0.83 nm/s, and 1.19 nm/s samples respectively. The slower deposited films have much taller hillocks (~16-18 nm), while the fastest deposited film has shorter ones (~7-8 nm). These changes in morphology are modest, as reflected by the small change in the mean hillock size, suggesting that morphology is not by itself responsible for the observed change in kinetic stability.

A widely accepted rule of thumb to avoid influence of surface roughness on nanoindentation measurements is to employ an indentation depth ~ 20 times the RMS roughness,

which we have done. Given that precaution and the small differences in the size of the hillocks, it seems unlikely that surface roughness is the major cause of the differences in mechanical properties amongst the films measured by nanoindentation. However, the ribbon has a smoother surface because it was polished before nanoindentation testing, so some of the difference between the ribbon and the films may be attributable to surface roughness.

B. Fluctuation electron microscopy and angular correlations

Fig. A3 shows all the average angular power spectra for n = 1 to n = 10. n = 1 corresponds to single speckles without symmetry-related partners, presumably arising from ordered arrangements of atoms that satisfy a pseudo-Bragg condition on one side of the optic axis (*i.e.* +**g**) but not the other side of the optic axis (*i.e.* -**g**). n = 2 are Friedel pairs. Odd orders $n \ge 3$ arise from some chance correlation of speckles arising from random overlap of ordered structures along the beam direction through the TEM sample thickness. Even orders $n \ge 4$ can have some contribution from random correlations but can also arise from rotational symmetries of single ordered regions. Because the even n symmetries are systematically higher power than the odd n symmetries, we interpret the even n symmetries as arising from real rotational symmetries in the material [38].

References

- [1] S. F. Swallen, K. L. Kearns, M. K. Mapes, Y. S. Kim, R. J. McMahon, M. D. Ediger, T. Wu, L. Yu, and S. Satija, *Organic Glasses with Exceptional Thermodynamic and Kinetic Stability*, Science (80-.). **315**, 353 (2007).
- [2] L. Berthier, P. Charbonneau, E. Flenner, and F. Zamponi, *Origin of Ultrastability in Vapor-Deposited Glasses*, Phys. Rev. Lett. **119**, 188002 (2017).
- [3] H. B. Yu, Y. Luo, and K. Samwer, *Ultrastable Metallic Glass*, Adv. Mater. **25**, 5904 (2013).
- [4] D. P. B. Aji, A. Hirata, F. Zhu, L. Pan, K. M. Reddy, S. Song, Y. Liu, T. Fujita, S. Kohara, and M. Chen, *Ultrastrong and Ultrastable Metallic Glass*, ArXiv Prepr. 1 (2013).
- [5] D. J. Magagnosc, G. Feng, L. Yu, X. Cheng, and D. S. Gianola, *Isochemical Control over Structural State and Mechanical Properties in Pd-Based Metallic Glass by Sputter Deposition at Elevated Temperatures*, APL Mater. **4**, 086104 (2016).
- [6] S. Y. Liu, Q. P. Cao, X. Qian, C. Wang, X. D. Wang, D. X. Zhang, X. L. Hu, W. Xu, M. Ferry, and J. Z. Jiang, *Effects of Substrate Temperature on Structure, Thermal Stability and Mechanical Property of a Zr-Based Metallic Glass Thin Film*, Thin Solid Films **595**, 17 (2015).
- [7] J. H. Chu, H. W. Chen, Y. C. Chan, J. G. Duh, J. W. Lee, and J. S. C. Jang, *Modification of Structure and Property in Zr-Based Thin Film Metallic Glass via Processing Temperature Control*, Thin Solid Films **561**, 38 (2014).

- [8] M. Lüttich, V. M. Giordano, S. Le Floch, E. Pineda, F. Zontone, Y. Luo, K. Samwer, and B. Ruta, *Anti-Aging in Ultrastable Metallic Glasses*, Phys. Rev. Lett. **120**, 135504 (2018).
- [9] P. Luo, C. R. Cao, F. Zhu, Y. M. Lv, Y. H. Liu, P. Wen, H. Y. Bai, G. Vaughan, M. di Michiel, B. Ruta, and W. H. Wang, *Ultrastable Metallic Glasses Formed on Cold Substrates*, Nat. Commun. **9**, 1389 (2018).
- [10] M. Liu, C. R. Cao, Y. M. Lu, W. H. Wang, and H. Y. Bai, *Flexible Amorphous Metal Films with High Stability*, Appl. Phys. Lett. **110**, 031901 (2017).
- [11] J. Q. Wang, Y. Shen, J. H. Perepezko, and M. D. Ediger, *Increasing the Kinetic Stability* of *Bulk Metallic Glasses*, Acta Mater. **104**, 25 (2016).
- [12] Y. Guo, A. Morozov, D. Schneider, J. W. Chung, C. Zhang, M. Waldmann, N. Yao, G. Fytas, C. B. Arnold, and R. D. Priestley, *Ultrastable Nanostructured Polymer Glasses*, Nat. Mater. 11, 337 (2012).
- [13] K. Zhang, Y. Li, Q. Huang, B. Wang, X. Zheng, Y. Ren, and W. Yang, *Ultrastable Amorphous Sb 2 Se 3 Film*, J. Phys. Chem. B **121**, 8188 (2017).
- [14] Q. Sun, D. M. Miskovic, K. Laws, H. Kong, X. Geng, and M. Ferry, *Transition towards**Ultrastable Metallic Glasses in Zr-Based Thin Films, Appl. Surf. Sci. **533**, 147453 (2020).
- [15] Y. Q. Cheng, E. Ma, and H. W. Sheng, *Atomic Level Structure in Multicomponent Bulk Metallic Glass*, Phys. Rev. Lett. **102**, 245501 (2009).
- [16] T. Fujita, K. Konno, W. Zhang, V. Kumar, M. Matsuura, A. Inoue, T. Sakurai, and M. W. Chen, *Atomic-Scale Heterogeneity of a Multicomponent Bulk Metallic Glass with*

- Excellent Glass Forming Ability, Phys. Rev. Lett. 103, 075502 (2009).
- [17] S. Hosokawa, J.-F. Bérar, N. Boudet, S. Kohara, W.-C. Pilgrim, M. Joester, J. Stellhorn, A. Zeidler, K. Maruyama, T. Nasu, W. Zhang, and H. Kato, A Partial Structure Factor Investigation of the Bulk Metallic Glass Zr 63 Ni 25 Al 12 as Studied by Using a Combination of Anomalous X-Ray Scattering and Reverse Monte Carlo Modeling, Int. J. Mater. Res. 103, 1108 (2012).
- [18] J. Hwang, Z. Melgarejo, Y. E. Kalay, I. Kalay, M. J. Kramer, D. S. Stone, and P. M. Voyles, *Nanoscale Structure and Structural Relaxation in Zr_{50}Cu_{45}Al_{5} Bulk Metallic Glass*, Phys. Rev. Lett. **108**, 195505 (2012).
- [19] A. Hirata, L. J. Kang, T. Fujita, B. Klumov, K. Matsue, M. Kotani, A. R. Yavari, and M. W. Chen, *Geometric Frustration of Icosahedron in Metallic Glasses.*, Science (80-.). **341**, 376 (2013).
- [20] P. Zhang, J. J. Maldonis, M. F. Besser, M. J. Kramer, and P. M. Voyles, *Medium-Range Structure and Glass Forming Ability in Zr–Cu–Al Bulk Metallic Glasses*, Acta Mater. **109**, 103 (2016).
- [21] J. Hwang, Z. H. Melgarejo, Y. E. Kalay, I. Kalay, M. J. Kramer, D. S. Stone, and P. M. Voyles, *Nanoscale Structure and Structural Relaxation in Zr50Cu45Al5 Bulk Metallic Glass*, Phys. Rev. Lett. **108**, 195505 (2012).
- [22] A. Hirata and M. W. Chen, Angstrom-Beam Electron Diffraction of Amorphous Materials,J. Non. Cryst. Solids 383, 52 (2014).

- [23] S. V. Muley, C. Cao, D. Chatterjee, C. Francis, F. P. Lu, M. D. Ediger, J. H. Perepezko, and P. M. Voyles, *Supplemental Material Varying Kinetic Stability, Icosahedral Ordering and Mechanical Properties of a Model Zr-Cu-Al Metallic Glass by Sputtering*, Phys. Rev. Mater. (2021).
- [24] J. Hwang, *Doctoral Thesis*, University of Wisconsin-Madison (2011).
- [25] X. Chen and J. J. Vlassak, Numerical Study on the Measurement of Thin Film Mechanical Properties by Means of Nanoindentation, J. Mater. Res. 16, 2974 (2001).
- [26] M. Ghidelli, S. Gravier, J. J. Blandin, P. Djemia, F. Mompiou, G. Abadias, J. P. Raskin, and T. Pardoen, *Extrinsic Mechanical Size Effects in Thin ZrNi Metallic Glass Films*, Acta Mater. **90**, 232 (2015).
- [27] W. C. Oliver and G. M. Pharr, An Improved Technique for Determining Hardness and Elastic Modulus Using Load and Displacement Sensing Indentation Experiments, J. Mater. Res. 7, 1564 (1992).
- [28] D. Ma, A. D. Stoica, and X.-L. Wang, *Power-Law Scaling and Fractal Nature of Medium-Range Order in Metallic Glasses.*, Nat. Mater. **8**, 30 (2009).
- [29] D. Lee, B. Zhao, E. Perim, H. Zhang, P. Gong, Y. Gao, Y. Liu, C. Toher, S. Curtarolo, J. Schroers, and J. J. Vlassak, *Crystallization Behavior upon Heating and Cooling in Cu50Zr50 Metallic Glass Thin Films*, Acta Mater. **121**, 68 (2016).
- [30] J. Q. Wang, N. Chen, P. Liu, Z. Wang, D. V Louzguine-luzgin, M. W. Chen, and J. H. Perepezko, *The Ultrastable Kinetic Behavior of an Au-Based Nanoglass*, Acta Mater. **79**,

- 30 (2014).
- [31] W. L. Johnson, G. Kaltenboeck, M. D. Demetriou, J. P. Schramm, X. Liu, K. Samwer, C.
 P. Kim, and D. C. Hofmann, *Beating Crystallization in Glass-Forming Metals by Millisecond Heating and Processing*, Science (80-.). 332, 828 (2011).
- [32] S. Pogatscher, P. J. Uggowitzer, and J. F. Löffler, *In-Situ Probing of Metallic Glass Formation and Crystallization upon Heating and Cooling via Fast Differential Scanning Calorimetry*, Appl. Phys. Lett. **104**, 251908 (2014).
- [33] F. X. Bai, J. H. Yao, Y. X. Wang, J. Pan, and Y. Li, Crystallization Kinetics of an Au-Based Metallic Glass upon Ultrafast Heating and Cooling, Scr. Mater. 132, 58 (2017).
- [34] K. L. Kearns, M. D. Ediger, H. Huth, and C. Schick, *One Micrometer Length Scale Controls Kinetic Stability of Low-Energy Glasses*, J. Phys. Chem. Lett. **1**, 388 (2010).
- [35] M. M. J. Treacy, J. M. Gibson, L. Fan, D. J. Paterson, and I. McNulty, *Fluctuation Microscopy: A Probe of Medium Range Order*, Reports Prog. Phys. **68**, 2899 (2005).
- [36] J. M. Gibson, M. M. J. Treacy, T. Sun, and N. J. Zaluzec, *Substantial Crystalline Topology in Amorphous Silicon*, Phys. Rev. Lett. **105**, 1 (2010).
- [37] A. C. Y. Liu, M. J. Neish, G. Stokol, G. A. Buckley, L. A. Smillie, M. D. De Jonge, R. T. Ott, M. J. Kramer, and L. Bourgeois, *Systematic Mapping of Icosahedral Short-Range Order in a Melt-Spun Zr 36Cu64 Metallic Glass*, Phys. Rev. Lett. **110**, 1 (2013).
- [38] S. Im, Z. Chen, J. M. Johnson, P. Zhao, G. H. Yoo, E. S. Park, Y. Wang, D. A. Muller, and J. Hwang, *Direct Determination of Structural Heterogeneity in Metallic Glasses*

- *Using Four-Dimensional Scanning Transmission Electron Microscopy*, Ultramicroscopy **195**, 189 (2018).
- [39] K. L. Kearns, T. Still, G. Fytas, and M. D. Ediger, *High-Modulus Organic Glasses*Prepared by Physical Vapor Deposition, Adv. Mater. 22, 39 (2010).
- [40] B. Yang, C. T. Liu, and T. G. Nieh, *Unified Equation for the Strength of Bulk Metallic Glasses*, Appl. Phys. Lett. **88**, 221911 (2006).
- [41] P. Zhang, S. X. Li, and Z. F. Zhang, General Relationship between Strength and Hardness, Mater. Sci. Eng. A **529**, 62 (2011).
- [42] J. Saida, R. Yamada, and M. Wakeda, *Recovery of Less Relaxed State in Zr-Al-Ni-Cu Bulk Metallic Glass Annealed above Glass Transition Temperature*, Appl. Phys. Lett. **103**, 221910 (2013).
- [43] O. Haruyama, Y. Nakayama, R. Wada, H. Tokunaga, J. Okada, T. Ishikawa, and Y. Yokoyama, *Volume and Enthalpy Relaxation in Zr55Cu30Ni5Al10 Bulk Metallic Glass*, Acta Mater. **58**, 1829 (2010).
- [44] A. Rauf, C. Y. Guo, Y. N. Fang, Z. Yu, B. A. Sun, and T. Feng, *Binary Cu-Zr Thin Film Metallic Glasses with Tunable Nanoscale Structures and Properties*, J. Non. Cryst. Solids **498**, 95 (2018).
- [45] S. V. Ketov, R. Joksimovic, G. Xie, A. Trifonov, K. Kurihara, and D. V. Louzguine-Luzgin, *Formation of Nanostructured Metallic Glass Thin Films upon Sputtering*, Heliyon **3**, e00228 (2017).

- [46] D. Manova, J. W. Gerlach, and S. Mändl, *Thin Film Deposition Using Energetic Ions*, Materials (Basel). **3**, 4109 (2010).
- [47] K. L. Kearns, S. F. Swallen, M. D. Ediger, T. Wu, Y. Sun, and L. Yu, *Hiking down the Energy Landscape: Progress Toward the Kauzmann Temperature via Vapor Deposition*, J. Phys. Chem. B 112, 4934 (2008).
- [48] N. Chen, D. V. Louzguine-Luzgin, G. Q. Xie, P. Sharma, J. H. Perepezko, M. Esashi, A. R. Yavari, and A. Inoue, Structural Investigation and Mechanical Properties of a Representative of a New Class of Materials: Nanograined Metallic Glasses, Nanotechnology 24, 045610 (2013).
- [49] G. B. Bokas, L. Zhao, D. Morgan, and I. Szlufarska, *Increased Stability of CuZrAl Metallic Glasses Prepared by Physical Vapor Deposition*, J. Alloys Compd. **728**, 1110 (2017).
- [50] Y. Q. Cheng, E. Ma, and H. W. Sheng, *Alloying Strongly Influences the Structure, Dynamics, and Glass Forming Ability of Metallic Supercooled Liquids*, Appl. Phys. Lett. **93**, 10 (2008).
- [51] F. H. . Zetterling, M. Dzugutov, and S. . Simdyankin, Formation of Large-Scale

 Icosahedral Clusters in a Simple Liquid Approaching the Glass Transition, J. Non. Cryst.

 Solids 293–295, 39 (2001).
- [52] M. Dzugutov, S. I. Simdyankin, and F. H. M. Zetterling, *Decoupling of Diffusion from Structural Relaxation and Spatial Heterogeneity in a Supercooled Simple Liquid*, Phys. Rev. Lett. **89**, 195701 (2002).

- [53] A. L. Greer, Y. Q. Cheng, and E. Ma, Shear Bands in Metallic Glasses, Mater. Sci. Eng. R74, 71 (2013).
- [54] M. M. Trexler and N. N. Thadhani, Mechanical Properties of Bulk Metallic Glasses, Prog. Mater. Sci. 55, 759 (2010).
- [55] Z. H. Melgarejo, J. E. Jakes, J. Hwang, Y. E. Kalay, M. J. Kramer, P. M. Voyles, and D.
 S. Stone, Variation of Hardness and Modulus across the Thickness of Zr-Cu-Al Metallic Glass Ribbons, MRS Proc. 1520, mrsf12 (2012).
- [56] Y. Q. Cheng, A. J. Cao, and E. Ma, Correlation between the Elastic Modulus and the Intrinsic Plastic Behavior of Metallic Glasses: The Roles of Atomic Configuration and Alloy Composition, Acta Mater. 57, 3253 (2009).
- [57] H. L. Peng, M. Z. Li, and W. H. Wang, Structural Signature of Plastic Deformation in Metallic Glasses, Phys. Rev. Lett. **106**, 135503 (2011).
- [58] P. Guan, M. Chen, and T. Egami, *Stress-Temperature Scaling for Steady-State Flow in Metallic Glasses*, Phys. Rev. Lett. **104**, 205701 (2010).

Figures

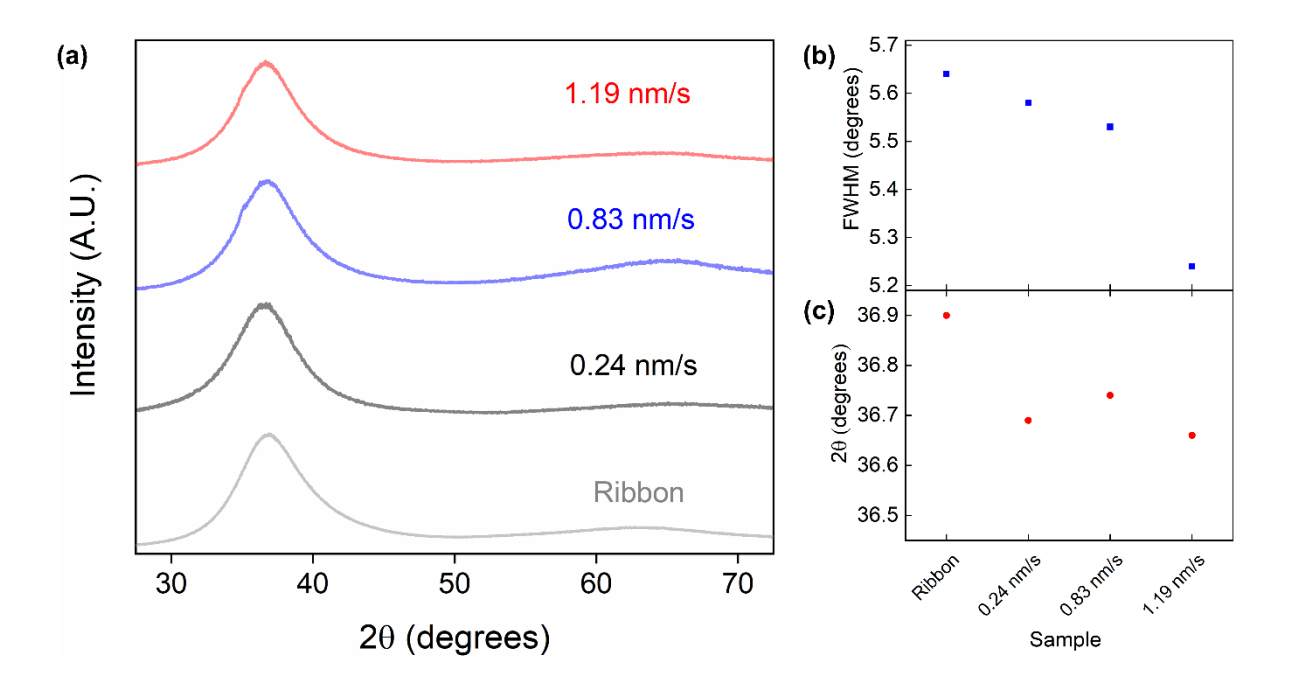


Fig. 1: (a) X-ray diffractograms are shown for ribbon and thin films (offset for clarity). (b) FWHM and (c) First broad diffraction peak positions for the thin film and ribbon samples.

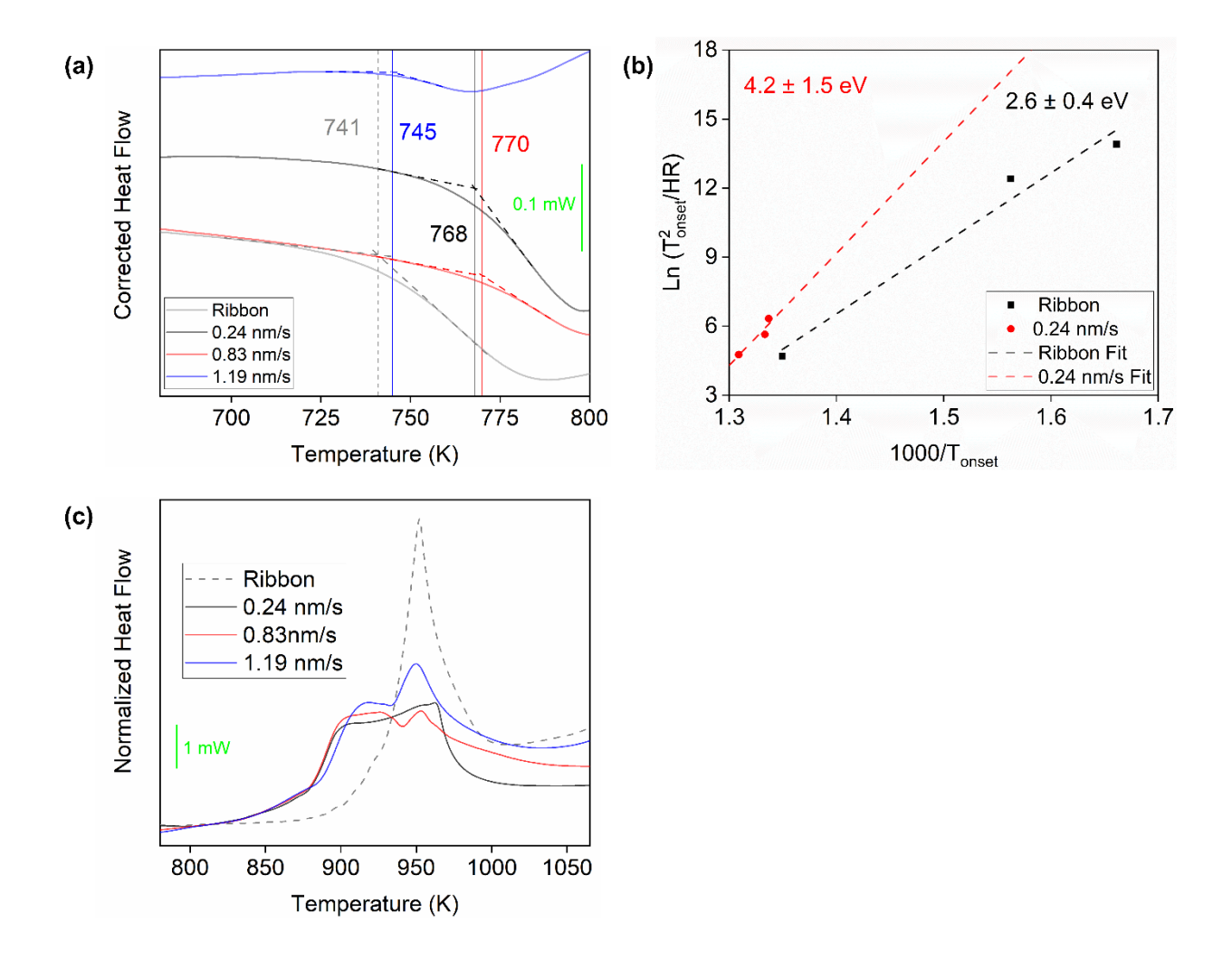


Fig. 2: Calorimetry data at a heating rate of 5000 K/s showing (a) T_{onsets} values. (b) Kissinger analysis for thin film grown at 0.24 nm/s and ribbon sample is shown. (c) shows crystallization behavior at 5000 K/s. Raw data have been smoothed and background-subtracted as described in the Experimental Details section.

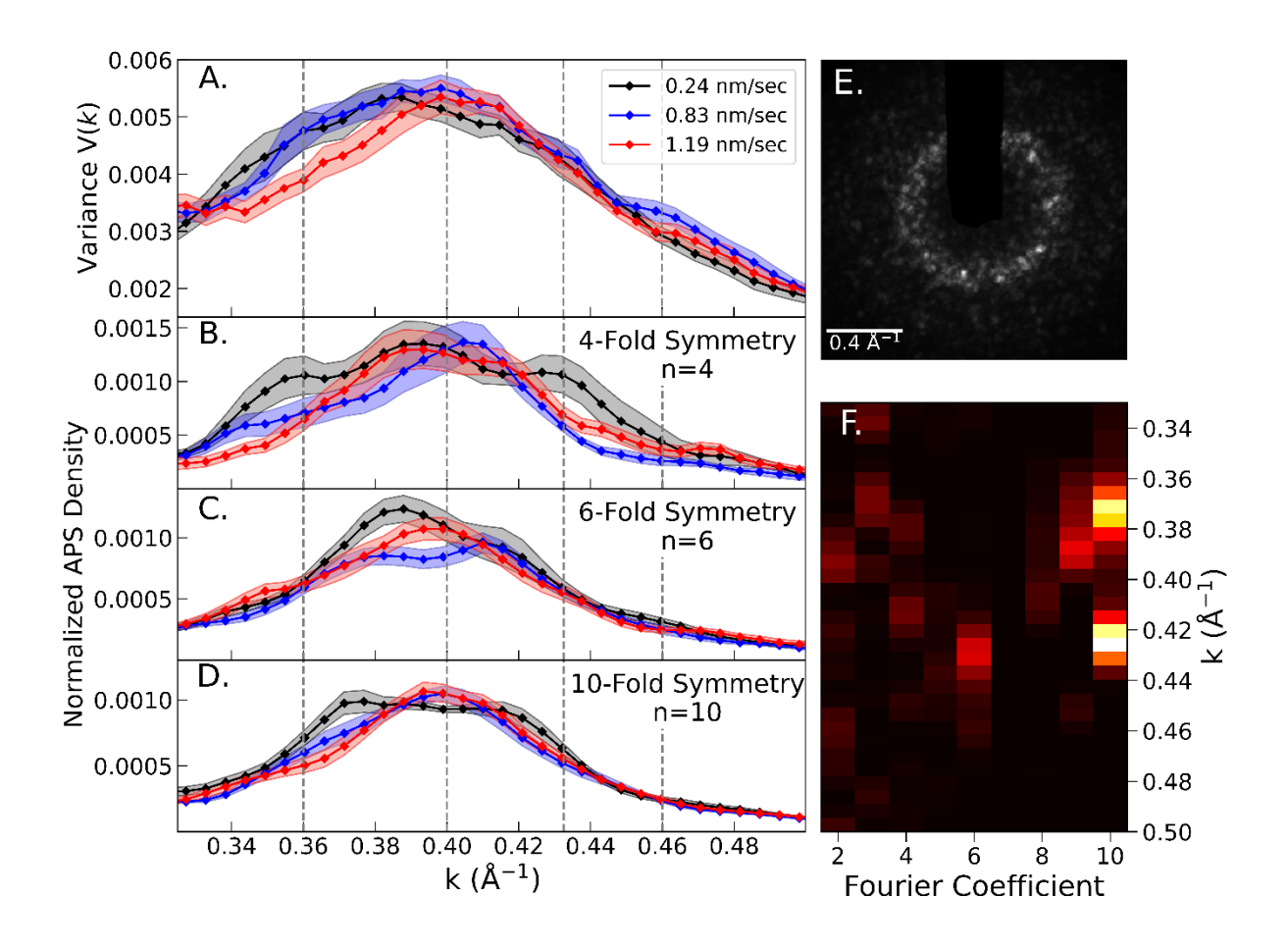


Fig. 3: (a) V(k) measured $Zr_{65}Cu_{27.5}Al_{7.5}$ MG films deposited at different deposition rates. Normalized average power spectral density of the (b) 4-fold, (c) 6-fold and (d) 10-fold rotational symmetry in nanodiffraction for all samples. (e) An example nanodiffraction pattern showing the polar coordinates (k, φ) used in Eq. 2. (f) The power spectrum of the pattern in (e) showing strong 10-fold symmetry.

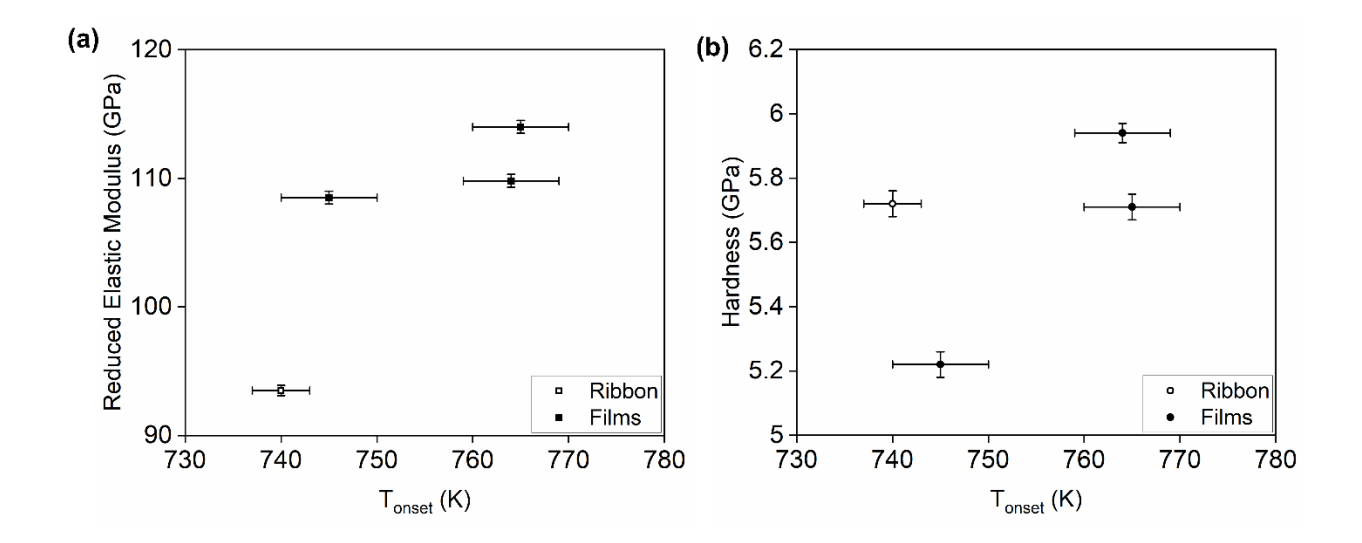


Fig. 4: (a) Reduced elastic moduli and (b) hardness vs T_{onset} for thin films and ribbon samples are shown.

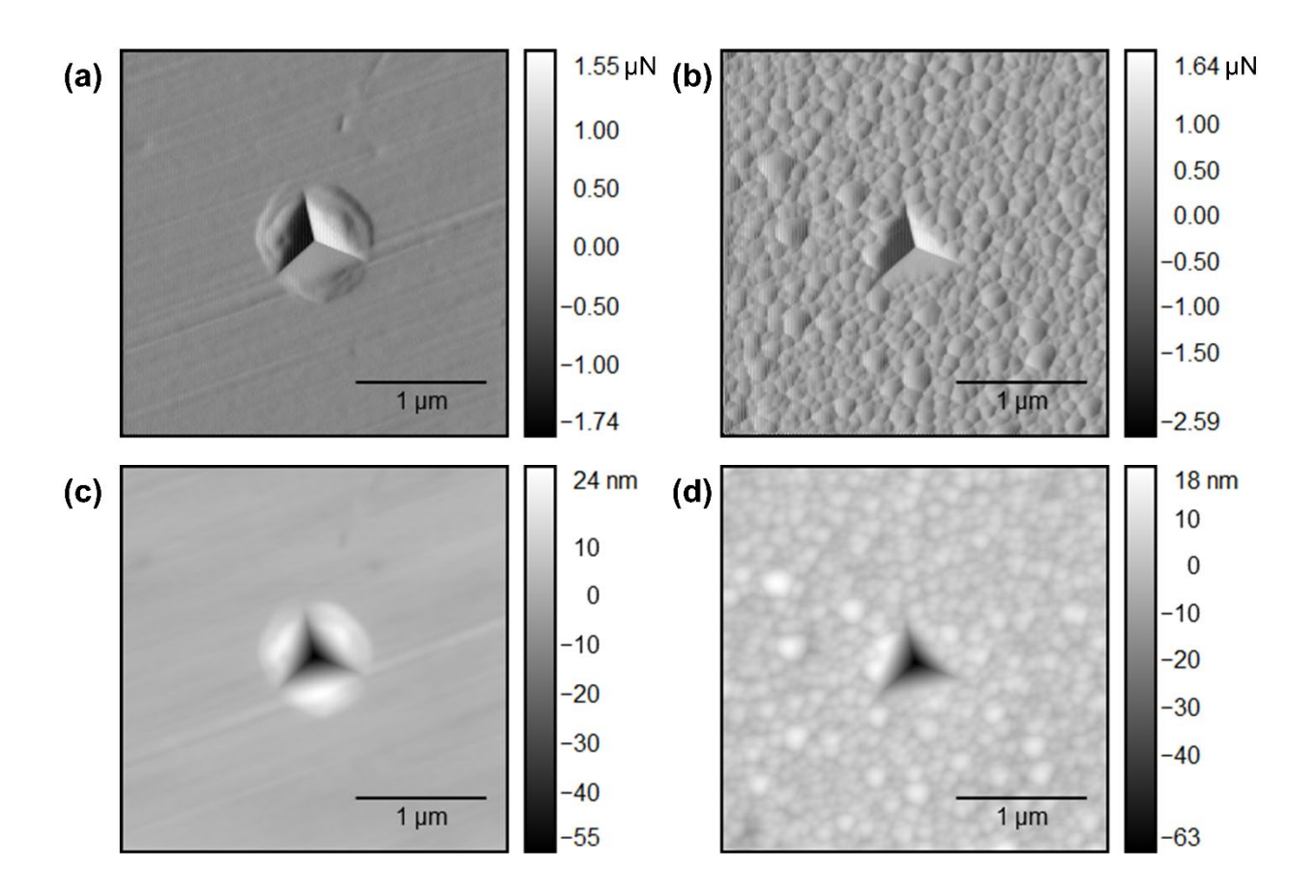


Fig. 5: (a) and (b) show gradient force images (scanning set point error) while (c) and (d) show two-dimensional surface maps for ribbon and the $\sim 3~\mu m$ thick film grown at a deposition rate of 0.83 nm/s respectively.

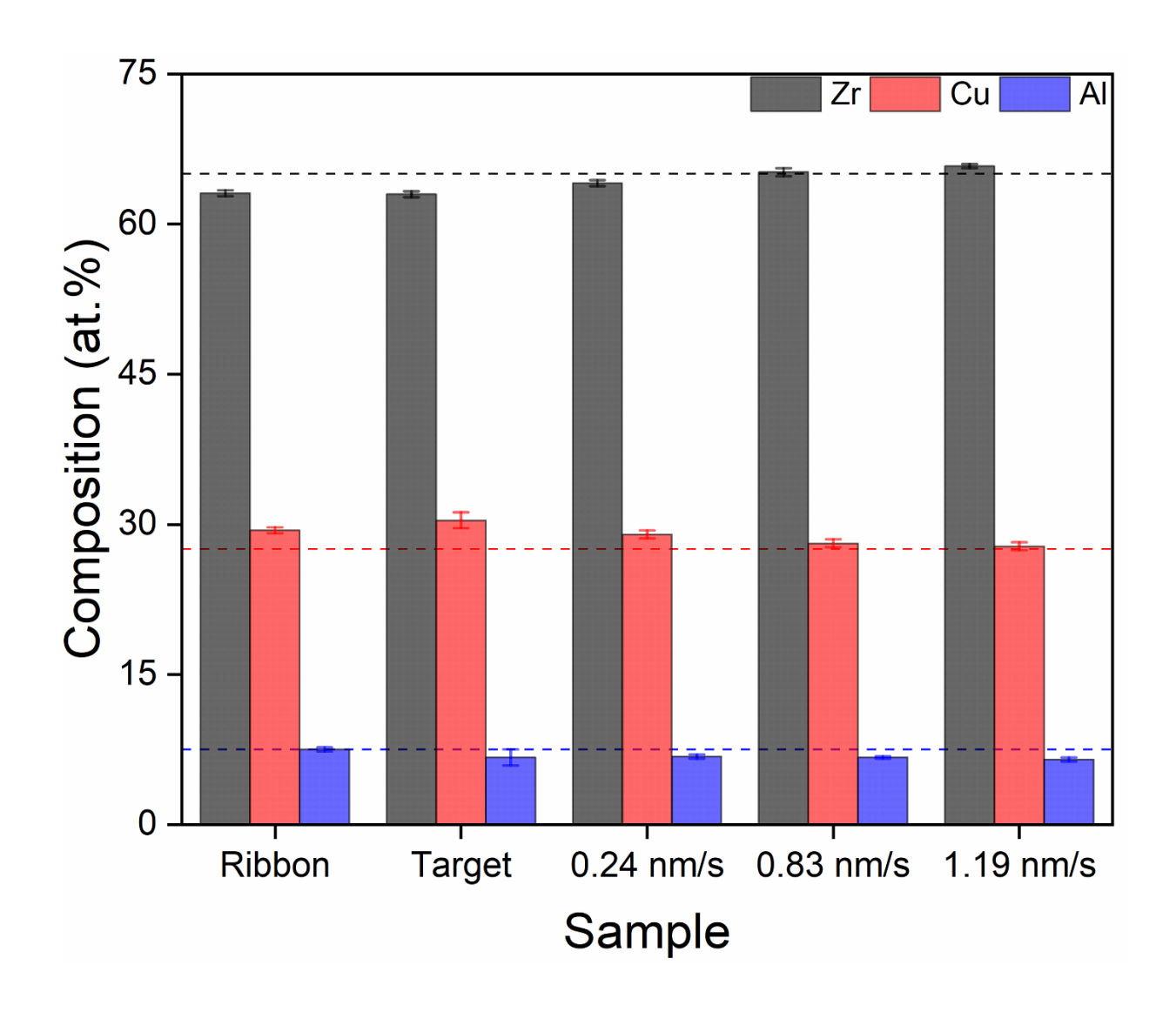


Fig. A1: Compositions of ribbon, thin films and target source as measured by SEM-EDS are shown. Dashed lines represent nominal alloy composition.

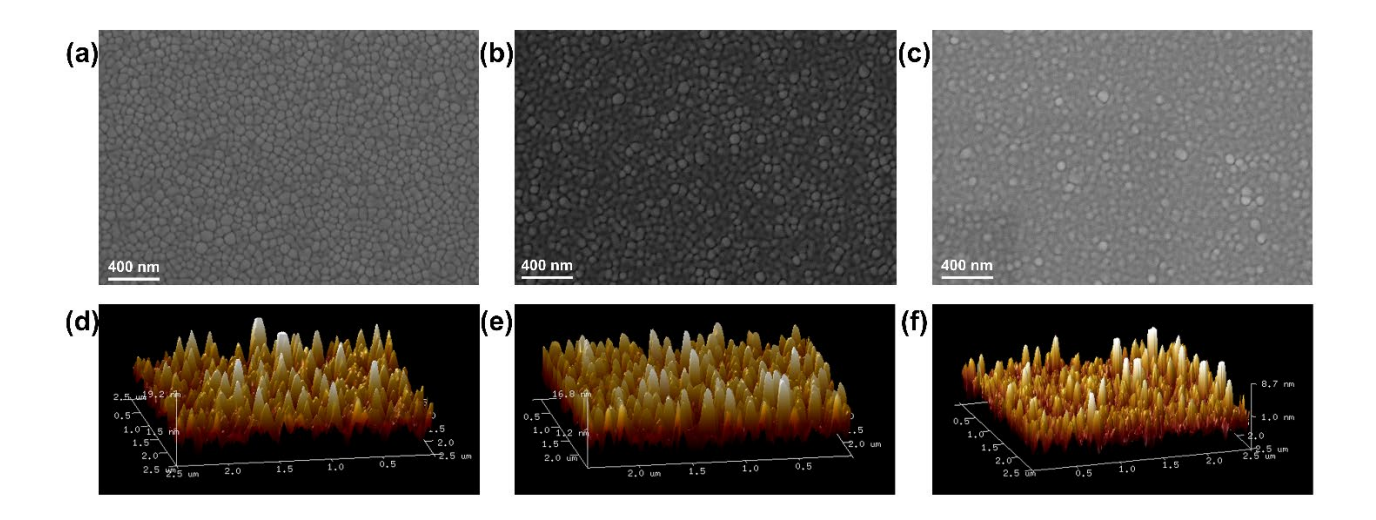


Fig. A2: Plan view SEM (top) and AFM images (bottom) of thin films grown at deposition rates of (a) 0.24, (b) 0.83 and (c) 1.19 nm/s.

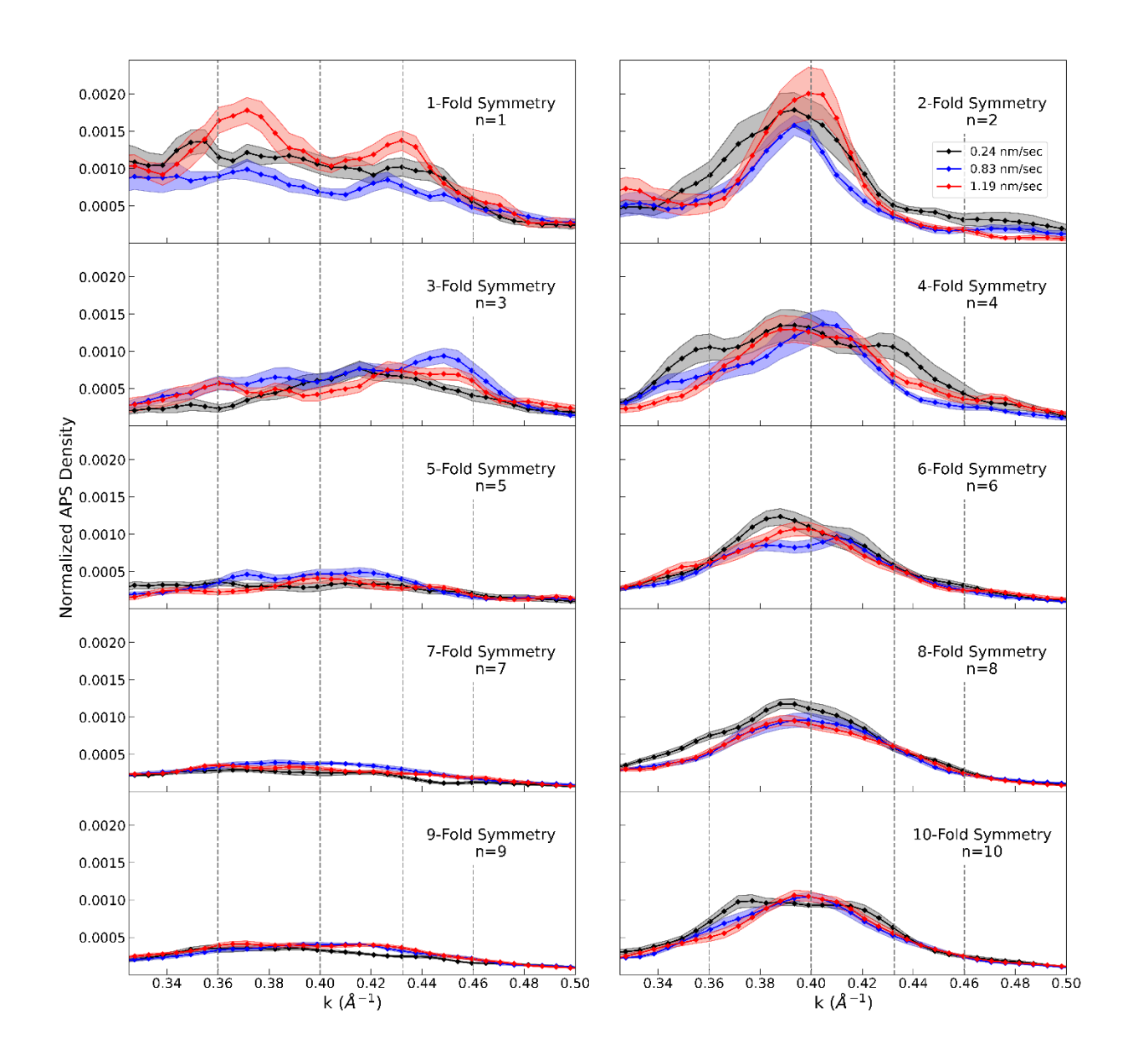


Fig. A3: Average angular power spectrum for n = 1 to 10 for all three samples with the same vertical scale for every order.

Supporting Information

Varying Kinetic Stability, Icosahedral Ordering, and Mechanical Properties of a Model Zr-Cu-Al Metallic Glass by Sputtering

Sachin V. Muley ¹, Chengrong Cao ¹, Debaditya Chatterjee ¹, Carter Francis ¹, Felix P. Lu ^{2,3}, Mark D. Ediger ⁴, John H. Perepezko ¹, and Paul M. Voyles ^{1,*}

¹ Department of Materials Science & Engineering, University of Wisconsin-Madison, 1509 University Avenue, Madison, WI 53706, United States of America

² Grainger Institute of Engineering, University of Wisconsin-Madison, 1550 Engineering Drive, Madison, WI 53706, United States of America

³ Present address – The Pritzker School of Molecular Engineering, University of Chicago, 5640 South Ellis Avenue, Chicago, IL 60637, United States of America

⁴ Department of Chemistry, University of Wisconsin-Madison, 1101 University Avenue, Madison, WI 53706, United States of America

Corresponding author: Paul M. Voyles

Author contact information:

Sachin V. Muley (<u>muley@wisc.edu</u>)

Chengrong Cao (ccao32@wisc.edu)

Debaditya Chatterjee (dchatterjee6@wisc.edu)

Carter Francis (csfrancis@wisc.edu)

Felix P. Lu (fplu@uchicago.edu)

Mark D. Ediger (ediger@chem.wisc.edu)

John H. Perepezko (perepezk@wisc.edu)

Paul M. Voyles (paul.voyles@wisc.edu, +1 (608) 265-7273)

Additional experimental details

A. Preliminary materials characterization

A Bruker D8 Discover X-ray diffractometer (XRD) equipped with a Cu- K_{α} source and area detector was used in the coupled Θ -2 Θ setting for structure studies of the thin films and ribbon samples. The relatively thick film samples were cleaved, and their cross-section was studied with Zeiss Leo-1530 field emission scanning electron microscope (SEM) to reveal thickness and fracture morphology at a gun energy of 3 kV. Dividing the thickness by deposition time gave an estimated deposition rate. An energy dispersive spectrometer (EDS) mounted on the SEM, was used to analyze the compositions of grown films. The EDS measurements were made at a working distance of 9 mm, gun energy of 15 kV and $1000 \times$ magnification. A Bruker BioAFM atomic force microscope (AFM) was used in contact mode at a scan rate of 0.7 Hz to study surface features and flatness of the thin films.

B. High rate calorimetry

The thermal properties of thin films and ribbons were measured by a high rate differential scanning calorimeter (Flash DSC 2+, Mettler Toledo) at a heating rate of 5000 K/s. Samples were scraped off with razor blades and carefully mounted onto flash DSC chips. Sample masses were very roughly estimated to be between 10 ng and 1 µg. Ar gas was flowed continuously during heating at 60 ml/min to prevent sample oxidation during measurement. For the DSC traces reported in Fig. 2(a), raw data was processed in the following manner: first, Savitzky-Golay smoothing with 20-point window was applied. Then, straight lines were fitted for the data range 360 – 375 K and subtracted from heat flow data. Finally, the heat flow traces were vertically offset to have zero heat flow at 360 K. For the DSC traces reported in Fig. 2(b), after smoothing, subtraction of straight

line and zeroing at 360 K, the area under the crystallization peak was calculated, then the curves were offset to zero at 815 K (supercooled region of all samples) and normalized so that all curves have the same area under the curve to account for differences in sample volume. T_{onset} values in Fig. 4 were averaged from 3-4 measurements.

C. Fluctuation electron microscopy and angular correlations

Approximately 20 nm thin film samples for FEM measurements were grown directly on electron-transparent Si₃N₄ membranes. The FEM measurements were made in a FEI Titan STEM with a CEOS probe C_s aberration corrector at 200 kV. The extraction voltage value for the Schottky emission gun was set at 4500 V. Microprobe mode with an extended Q range was used in the FEI control software. Operating in energy filtered STEM (EF-STEM), a camera length of 512 mm and a 10 eV wide slit were chosen. STEM images and nanodiffraction patterns were simultaneously acquired via a Gatan annular dark-field detector mounted on a 2.5 mm GIF entrance aperture. An acceptable diffraction focus was maintained by adjusting the diffraction lens current using FEI free-lens control interface. An exposure time of 6 s ensured a reasonably high signal to noise ratio in each diffraction pattern. By employing a CCD binning of 4 on a 10 × 10 grid of positions, 512 × 512 pixel nanodiffraction patterns were acquired across 30 × 30 nm² sample area. Variance data from 10 different sample regions was averaged and reported with one standard deviation of mean error bars. Sample thickness was calculated by applying the log-ratio method to elastic scattering transmittance. The samples had an electron transmittance of 55 - 65 %, which is thin enough for FEM and angular correlations experiments [1]. For our measurements, we chose a probe size of 2 nm, C2 aperture size of 10 μm, convergence angle of 0.6 mrad, spot number 7, and probe current of 3.36 pA [2]. V(k) data is not corrected for surface oxide on the surface of thin films. Angular correlation analysis was performed on the same set of nanodiffraction patterns. The angular

correlation $C(k, \phi)$ was computed for each pattern, then averaged for each sample area. The power spectrum for each area was computed from the averaged C. Fig. 3 reports the power spectrum averaged over 10 different samples areas with one standard deviation of the mean error bars.

D. Nanoindentation

Indentation measurements were made by a diamond Berkovich tip mounted onto a Hysitron TI950 instrument. Before testing, the tip area function was calibrated against a fused silica standard sample and the thin film specimen were superglued onto magnetic pucks. Measurements on the standard sample were made to verify acceptable E_r (68 - 71 GPa) and H (9.1 – 9.3 GPa) values, indicating the instrument was well-calibrated. The indent depth was restricted to <12% of the film thickness to avoid substrate effects [3,4]. Optimum indent contact depths for all thin films were found to be 0.08 - 0.12 times the thin film thickness since E_r and H values plateaued by employing a partial load-unload function: a small force was applied by the nanoindentation probe, withdrawn, and then a slightly higher force was applied, withdrawn, and so on for a prescribed number of cycles. To ensure a consistent comparison, an optimum load was adjusted for each thin film sample (1.5 mN for films grown at 0.24 and 0.83 nm/s and 1 mN for the one grown at 1.19 nm/s) such that the indentation contact depth was controlled to be 10 % of the film thickness. The nanoindentation measurements were made under basic trapezoid loading function at room temperature. At least 25 indents were performed on each thin film sample and the reduced elastic modulus (E_r) and hardness (H) values were reported as means and standard errors of the mean. E_r and H values were calculated using the Oliver-Pharr method of unloading curve analysis in the Triboscan software [5]. For comparison, nanoindentation tests under loadcontrol mode at peak load of 1.5 mN were performed on a melt-quenched ribbon sample with the same nominal composition. The ribbon sample was clamped edge-on between two steel clamps

and cloth-polished to $0.03~\mu m$. Nanoindentation data on bulk ribbon sample were corrected for pileups. Indents were imaged by scanning probe microscopy setting in the Hysitron TI950 indenter at a set point of $2~\mu N$. The surface tilt was satisfactorily removed by the average plane subtraction feature available in the TriboView software. Nanoindentation data on the bulk ribbon sample were corrected for pileups by measuring the real contact area from post-indent images using ImageJ.

References

- [1] J. Hwang, *Doctoral Thesis*, University of Wisconsin-Madison (2011).
- [2] P. Zhang, J. J. Maldonis, M. F. Besser, M. J. Kramer, and P. M. Voyles, *Medium-Range Structure and Glass Forming Ability in Zr–Cu–Al Bulk Metallic Glasses*, Acta Mater. **109**, 103 (2016).
- [3] X. Chen and J. J. Vlassak, Numerical Study on the Measurement of Thin Film Mechanical Properties by Means of Nanoindentation, J. Mater. Res. 16, 2974 (2001).
- [4] M. Ghidelli, S. Gravier, J. J. Blandin, P. Djemia, F. Mompiou, G. Abadias, J. P. Raskin, and T. Pardoen, *Extrinsic Mechanical Size Effects in Thin ZrNi Metallic Glass Films*, Acta Mater. **90**, 232 (2015).
- [5] W. C. Oliver and G. M. Pharr, An Improved Technique for Determining Hardness and Elastic Modulus Using Load and Displacement Sensing Indentation Experiments, J. Mater. Res. 7, 1564 (1992).